Hindawi
Shock and Vibration
Volume 2022, Article ID 9285908, 16 pages
https://doi.org/10.1155/2022/9285908

Research Article

Dynamic Failure Characteristics of Combination Rock under Different Strain Rates: Insights from SHPB Tests

Pingfeng Li,[1] **Mingjian Huang**,[2,3] **Junji Lu**,[3] **Heping Xia**,[4] **Jinquan Wu**,[5] **and Zhengliang Li**[6]

[1]*Hongda Blasting Engineering Group Co., Ltd., Guangzhou 510623, China*
[2]*School of Resources and Safety Engineering, Central South University, Changsha 410083, China*
[3]*Hunan Lianshao Construction Engineering (Group) Co., Ltd., Changsha 410011, China*
[4]*Fujian Xinhuadu Engineering Co., Ltd., Xiamen 361000, China*
[5]*Lincang Transportation Bureau of Yunnan Province, Lincang 677099, China*
[6]*School of Civil Engineering, Southeast University, Nanjing 210096, China*

Correspondence should be addressed to Jinquan Wu; 87507761@qq.com and Zhengliang Li; lzllyy92@163.com

Received 4 April 2022; Accepted 10 May 2022; Published 28 May 2022

Academic Editor: Tao Meng

In order to investigate the dynamic mechanical behavior of composite rock in deep-buried tunnels, the dynamic impact tests of the combinations with three lithologies (granite-H, cyan sandstone-S1, and red sandstone-S2) and six kinds of composite forms (H-S1, S1-H, H-S2, S2-H, S1-S2, and S2-S1), were carried out in this study. Additionally, the effects of the combination forms and strain rates on the stress-strain curve, peak stress, energy utilization rate (EUR), failure process, displacement field, and failure mode of the composite sample were analyzed. The results show that the peak stresses of all the combinations are linearly and positively correlated with the strain rate. When the strain rate is close, the peak stress and elastic modulus of the combination with front hard and rear soft (FHRS) rocks are larger. Furthermore, the EUR of different combinations is proportional to the incident energy. The EUR of the front soft and rear hard (FSRH) combination is generally higher than that of the FHRS combination. In general, the rock with low strength always fails first in the composite. When the strength disparity between the two rocks of the composite is small, the failure of the composite with FSRH is relatively small, and the main deformation occurs in the rock with low strength. Finally, the fractal dimension of the fragments after the impact of the FSRH combination is larger, i.e., the lumpiness of fragments is closer.

1. Introduction

At present, the exploitation of mineral resources and the underground space utilization gradually shift to the deep [1–4]. The increase in ground stresses after entering the deep regions may cause frequent coal bursts [5], large deformations of roadways [6, 7], rock bursts [8], and other disasters [9], which greatly impact the stability of deep rock engineering [10–16]. As shown in Figure 1, the surrounding rock of deep-buried tunnels may not only contain one lithology. The combination relationship between different lithologic rock mass to a great extent determines the stability and failure mode of engineering rock mass, and the dynamic disturbances, such as fault dislocation and blasting vibration in underground engineering, are more frequent. Therefore, it is critical to explore the failure mechanism of rock combinations formed by different lithologies under dynamic loads for evaluating the state of the surrounding rock and formulating the targeted support measurement [17].

Many researchers have carried out extensive research studies on the mechanical behavior of combination rocks. However, the main focus has remained on the static mechanical properties of the coal-rock combination. Liu et al. [18] analyzed the influence and failure mechanism of rock strength on the mechanical characteristics and failure mode by uniaxial compression (UC) tests of rock-coal-rock samples with different rock strengths, and evaluated the

Figure 1: Photograph of composite rock in tunnel face.

influence of rock strength on coal instability. Wang et al. [19], Pan et al. [20], and Li et al. [21] analyzed the deformation characteristics and failure modes of the coal-rock combinations with different coal-rock height ratios based on UC and uniaxial cyclic loading tests, and assessed the differences in mechanical properties and energy evolution characteristics. Tao et al. [22] analyzed the stress characteristics and mechanical properties of the coal-rock combinations. The similarities and differences of the deformation and failure characteristics between the composite coal and soft-hard coal were compared. Cheng et al. [23] defined and deduced the theoretical calculation relation of the corresponding mechanical index of composite rock and verified it through laboratory tests. Zhang et al. [24] carried out an in-depth analysis of the influence of coal thickness on the mechanical behavior of rock-coal-rock by UC tests combined with numerical simulations. Liu et al. [25] established the constitutive damage model of two kinds of coal and analyzed the influence mechanism of rock on coal mechanical behavior in the coal-rock combination.

Many research studies were also focused on the failure and lithological characteristics of the coal-rock combinations. Zuo et al. [26] carried out uniaxial and triaxial compression tests on rock, coal, and coal-rock combinations to obtain the failure mode and mechanical behavior of the coal-rock combinations under different stress conditions. Shen et al. [27], Xia et al. [28], and Tang et al. [29] analyzed the mechanical behavior and damage characteristics of the coal-rock combination with different inclination angles. The results showed that the peak strength and elastic modulus of the coal-rock combination were between rock and coal, and the elastic modulus and peak strength decreased with the increase in coal inclination angle. Lu et al. [30] studied the deformation, strength, and failure characteristics of layered coal-rock composition by a self-developed true triaxial loading system. Liu et al. [31] and Ma et al. [32] used the numerical simulation to analyze the influence of the relative height of two kinds of rocks on the microcracks' characteristics and established the corresponding constitutive model. Zhang et al. [33] defined six kinds of rock materials with different lithologic characteristics and used two combination methods to make cylinder specimens with different joint angles from 0° to 90°. The mechanical properties and failure modes of composite rock were also analyzed.

In terms of the studies of dynamic mechanical properties of the coal-rock composite, Li et al. [34], Miao et al. [35], and Pan et al. [36] used a split-Hopkinson pressure bar (SHPB) to carry out a dynamic impact test on coal-rock composite containing cracks. In this way, the dynamic mechanical properties and fractal characteristics of samples under different impact velocities were studied. The results showed that the strength and elastic modulus are the main reasons for the disparity in the mechanical properties between the two materials. Zuo et al. [37] conducted dynamic impact tests on coal-rock composites under different confining pressures, gas pressures, and loads to determine the mechanical behavior and failure mechanism. Dong et al. [38] and Lu et al. [39] analyzed the uniaxial compressive strength (UCS), elastic modulus, and stress-strain curve of rock-coal composite in detail, and explained the strength and deformation mechanism of rock-coal-rock samples from a microperspective.

Although many research studies on different attributes of rock and coal-rock combinations have been carried out earlier, the studies on the dynamic mechanical properties of rock combinations are sparse. Also, the existing studies primarily focus on the coal-rock combinations. However, few reports are on the dynamic mechanical properties and failure mechanism of rock-rock combinations in deep tunnels. Based on this, the SHPB tests of the combinations of granite, cyan sandstone, and red sandstone under different strain rates were carried out in this research study. The influence of strain rate and combination form on the dynamic mechanical properties of the combination from the aspects of the stress-strain curve, peak stress, energy absorption, failure process, full-field displacement, and block characteristics is discussed. This study provides a reference for the stability evaluation of complex engineering rock mass under dynamic loading.

2. Materials and Methods

2.1. Material. Three kinds of lithologies (granite, cyan sandstone, and red sandstone) of rock samples were selected to make a composite rock. The samples were collected from Shandong Province, China. The samples were processed into a cylinder (diameter and height both are 50 mm), as shown in Figure 2(a). Then, the circular sections of samples with different lithology were bonded by epoxy resin adhesive to form composite rock samples, as shown in Figure 2(b). Thus, there were a total of three combinations and eighteen samples. Figure 2(c) shows the distribution of mineral composition and relative content of three types of samples [40]. Among them, the quartz content of red sandstone is the highest (77.8%). Prior to the dynamic impact tests, the P-wave velocity, UCS, and elastic modulus of the three types of samples were determined. In terms of strength, granite has the highest strength, followed by cyan sandstone, whereas red sandstone has the least strength, which is about 43.3% of cyan sandstone. Table 1 enlists the

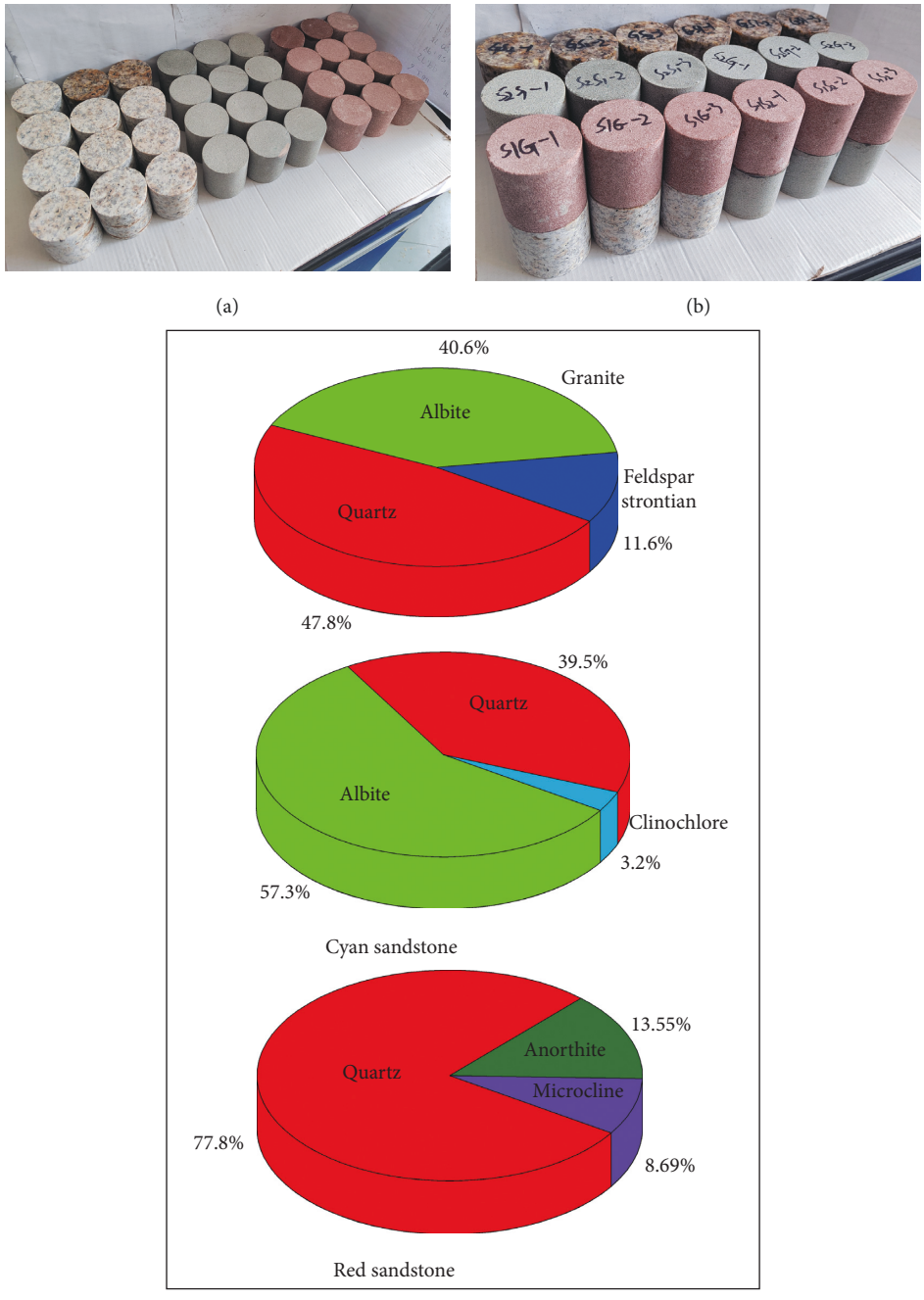

Figure 2: Photographs of test samples and mineral composition; (a) granite, cyan sandstone, and red sandstone samples; (b) composite samples; and (c) mineral composition and relative content.

Table 1: Physical and mechanical parameters of the specimen.

Specimen	P-wave velocity (m/s)	UCS (MPa)	Elastic modulus (GPa)
Granite (H)	3585.3	103.8	83.5
Cyan sandstone (S1)	2526.3	73.0	23.7
Red sandstone (S2)	2369.3	31.6	15.6
H-S1	2942.7	—	—
H-S2	2832.3	—	—
S1-S2	2421.7	—	—

Table 2: Dynamic mechanical parameters of composite specimens for SHPB test.

Specimen no.	Strain rate (s^{-1})	Peak stress (MPa)	W_i (J)	W_r (J)	W_t (J)	W_a (J)	η (%)
H-S1-0.3*	143.1	101.4	313.4	147.7	117.1	48.6	15.5
H-S1-0.35	200.7	148.7	371.0	180.2	114.4	76.4	20.6
H-S1-0.4	239.9	178.2	445.0	245.4	85.2	114.4	25.7
S1-H-0.3	165.4	113.5	264.2	181.6	49.5	33.1	13.0
S1-H-0.35	217.7	155.1	357.7	183.8	78.7	95.2	26.6
S1-H-0.4	252.1	188.1	511.8	229.2	86.8	195.8	42.2
H-S2-0.3	195.0	132.3	318.4	129.7	84.6	104.1	32.7
H-S2-0.35	202.4	141.2	356.1	188.1	23.4	144.6	40.6
H-S2-0.4	225.5	168.4	402.3	154.1	49.9	198.3	49.3
S2-H-0.3	172.8	113.1	254.4	112.2	65.9	76.3	30.0
S2-H-0.35	177.6	118.7	277.0	118.4	71.1	87.5	31.6
S2-H-0.4	217.7	149.3	365.6	185.5	15.6	164.5	45.0
S1-S2-0.3	165.8	102.3	294.2	190.7	59.1	44.4	15.1
S1-S2-0.35	230.3	130.0	387.9	220.2	76.2	91.5	23.6
S1-S2-0.4	246.9	144.5	453.3	275.1	43.6	134.6	29.7
S2-S1-0.3	179.8	107.5	275.4	157.4	64.3	53.7	19.5
S2-S1-0.35	216.8	113.1	349.1	224.0	45.9	79.2	22.7
S2-S1-0.4	230.8	117.1	377.6	247.1	38.0	92.5	24.5

*Note: the specimen no. H-S1-0.3, H means granite, S1 means cyan sandstone, and 0.3 means gas pressure.

specific values of the basic mechanical parameters. Table 1 also provides the P-wave velocities of composite rock samples, among which the P-wave velocity of granite-cyan sandstone assemblage is the highest (2942.7 m/s). As described in Table 2, three SHPB impact tests with different air pressures (0.3, 0.35, and 0.4 MPa) were carried out for six composite rocks (H-S1, S1-H, H-S2, S2-H, S1-S2, and S2-S1), a total of 18 tests.

2.2. SHPB Apparatus. Figure 3(a) shows the SHPB test system, and Figure 3(b) shows the schematic diagram of the system [40]. The system is equipped with an axial pressure and confining pressure loading device to realize a dynamic-static combined loading test. The sample failure process can be captured by a high-speed photography system with a maximum frame rate of up to 10,000 fps. The cylindrical punch (diameter is 50 mm), incident bar, transmission bar, and absorption bar of the test device are 50Cr steel, Young's modulus is 240 GPa, the density is 7,800 kg/m^3, the P-wave velocity in the bar is 5,580 m/s, and the wave impedance is 4.35×10^7 MPa/s. The rock strain signals were obtained by LK2109A super-dynamic strain gauge and LK2400 high-speed data collector. During the test, the BC-202 dual-channel detonation velocity meter was used to measure the velocity of the punch. The constant velocity impact was realized by controlling the pressure of the high-pressure chamber, and the velocity of the punch was changed by adjusting the impact pressure or reducing the depth of the punch into the chamber to achieve the required impact velocity.

2.3. Data Processing. For the SHPB test, the three-wave method [41] is one of the most commonly used methods for processing test data. Equation (1) shows the calculation formulae for stress, strain, and strain rate in the sample.

$$\begin{cases} \sigma_s = \dfrac{A_0 E_0}{2A_s}\left(\varepsilon_I + \varepsilon_R + \varepsilon_T\right), \\ \varepsilon_s = \dfrac{C_0}{l_s}\displaystyle\int_0^t \left(\varepsilon_I - \varepsilon_R - \varepsilon_T\right)\mathrm{d}t, \\ \dot{\varepsilon}_s = \dfrac{C_0}{l_s}\left(\varepsilon_I - \varepsilon_R - \varepsilon_T\right), \end{cases} \tag{1}$$

where σ_s, ε_s, and $\dot{\varepsilon}_s$ are the dynamic compressive stress, strain, and strain rate, respectively; A_0, E_0, and C_0 are the cross-sectional area, elastic modulus, and P-wave velocity of elastic bars; A_s and l_s are the cross-sectional area and length of the specimen; and ε_I, ε_R, and ε_T are incident, reflected, and transmitted wave signals.

2.3.1. Dynamic Stress Equilibrium. Whether the dynamic stress is balanced is an important premise to measure the effectiveness of the dynamic impact test, which can be corroborated by the time-history curves of the waveform. It can be seen from Figure 4 that the transmitted wave has a high degree of agreement with the sum of the incident and reflected waves, so it meets the premise of dynamic stress balance, i.e., the dynamic impact test of rock is effective.

2.3.2. Determination of Mechanical Parameters. Figure 5(a) shows the determination of peak stress and strain rate of the SHPB test data (specimen H-S1-0.4). The dynamic strength of the rock is the peak stress. Similarly, the strain rate also takes the maximum value of the strain rate. Additionally, the incident energy (W_i), reflected energy (W_r), and transmitted energy (W_t) of the stress waves can be determined using equations (2)–(4). In reference [42], according to the conservation of energy principle, the

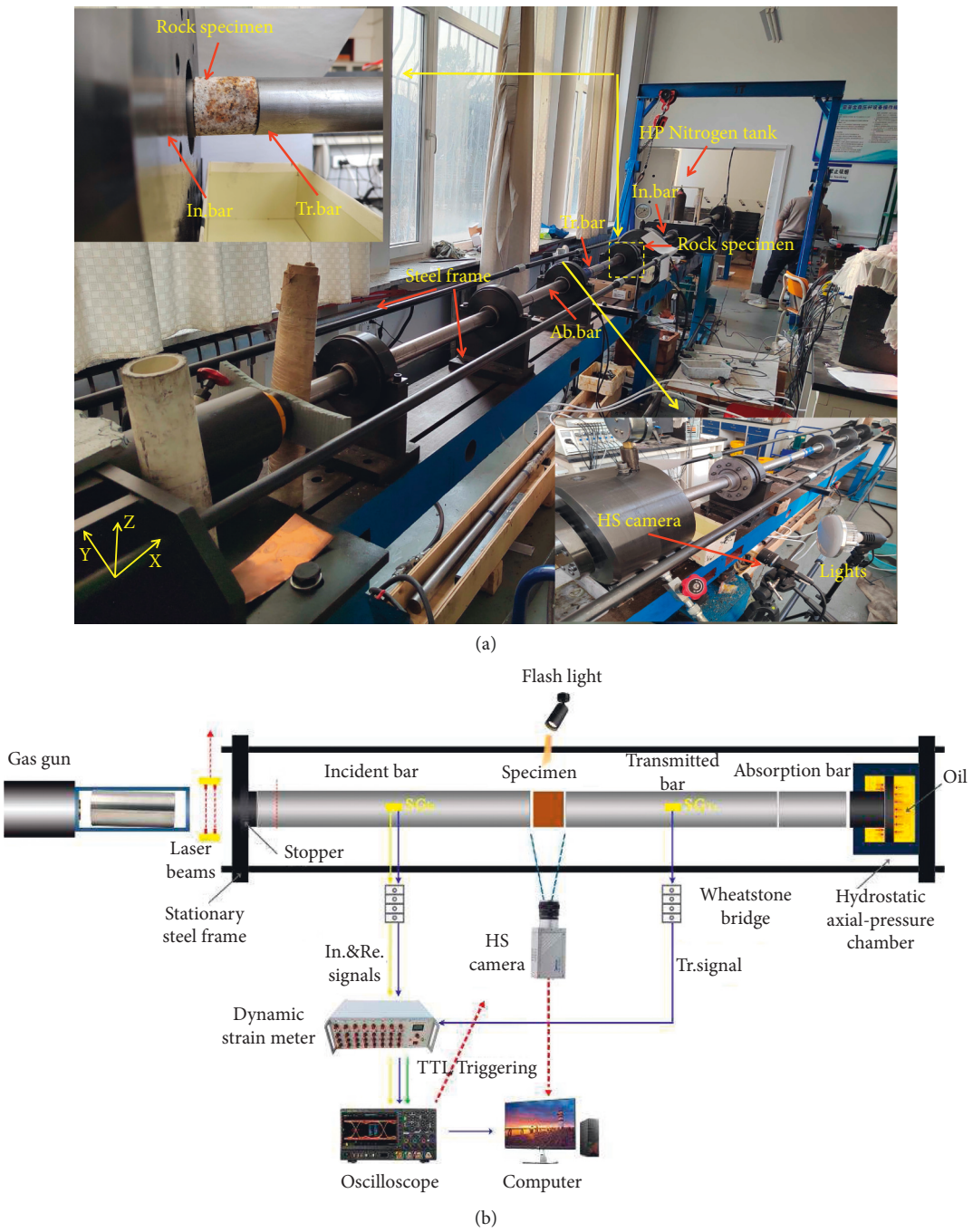

Figure 3: The SHPB test system; (a) photograph of SHPB device; and (b) schematic diagram of SHPB system.

absorbed energy (W_a) by rock specimens during impact tests can also be determined using equation (5). Figure 5(b) shows the variation of the four types of energies for the specimen H-S1-0.4 during an impact test. The variation process of all energies is the same, which increases at first and then tends to be stable. Also, the parameter (W_a/W_i) can be used to evaluate the energy utilization efficiency. In general, the absorbed energy by the brittle material mainly includes three parts: fracture energy (new crack production), heat and acoustic energy, and kinetic energy of the blocks; the last two parts only share low and can be negligible.

$$W_i = C_0 A_0 E_0 \int_0^\tau \varepsilon_I^2 \mathrm{d}t, \tag{2}$$

$$W_r = C_0 A_0 E_0 \int_0^\tau \varepsilon_R^2 \mathrm{d}t, \tag{3}$$

$$W_t = C_0 A_0 E_0 \int_0^\tau \varepsilon_T^2 \mathrm{d}t, \tag{4}$$

$$W_a = W_I - W_R - W_T. \tag{5}$$

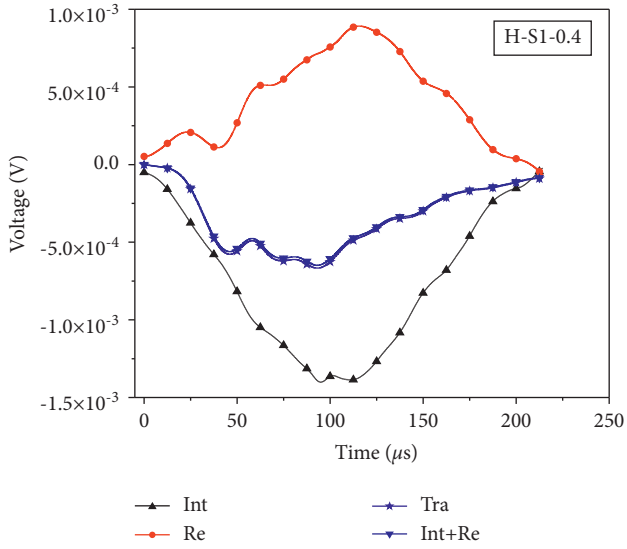

Figure 4: Dynamic stresses on both ends of the composite specimen.

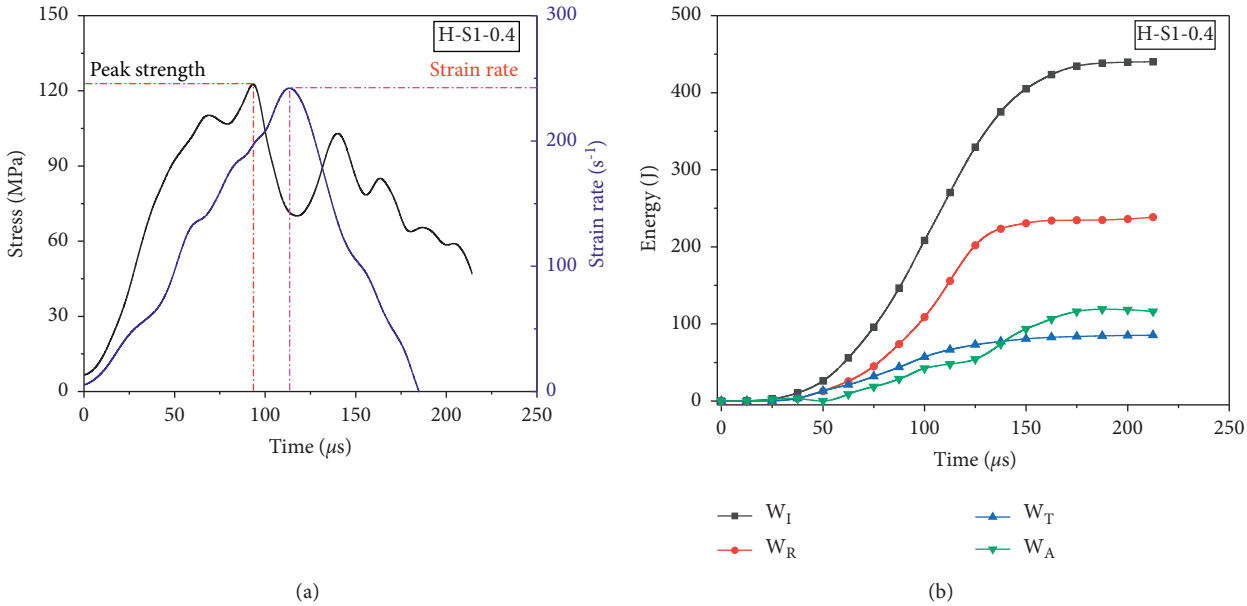

Figure 5: (a) Determination of peak stress and strain rate, and (b) energy evolution of specimen (H-S1-0.4).

3. Results and Discussion

3.1. Dynamic Properties

3.1.1. Mechanical Behavior. Figure 6(a) shows the typical stress-strain curve of the granite-cyan sandstone combination. When the gas pressure value is the same, the combination strain rate of S1-H is higher than that of H-S1, and the corresponding peak stress is higher. The typical stress-strain curve can be divided into four stages: I-elastic deformation stage, II-yield stage, III-strain-softening stage, and IV-rebound stage. The slope (dynamic elastic modulus) of the combination S1-H in the prepeak elastic stage is larger than H-S1, whereas the yield stage is shorter. Moreover, the stress drop in the postpeak strain-softening stage is more obvious for S1-H. However, there is a long platform in the late strain-softening stage of the combination H-S1. The rebound of the two combinations is the same, including the rebound deformation and modulus. As shown in Figure 6(b), the typical stress-strain curves of the other two forms of the composite are presented. The variation characteristics of the samples with closer strain rates are also illustrated here. Overall, for the two different combination forms formed by the two lithologies, when the strain rate is close, the peak stress of the composite with the lower UCS of rock in the front (i.e., first contact with the incident stress wave) is lower. The strain corresponding to the peak stress is higher, and the dynamic elastic modulus is reduced.

3.1.2. Strength Characteristics. The peak stresses of the composite samples under different strain rates are shown in Figure 7, while the specific values of strain rates and peak

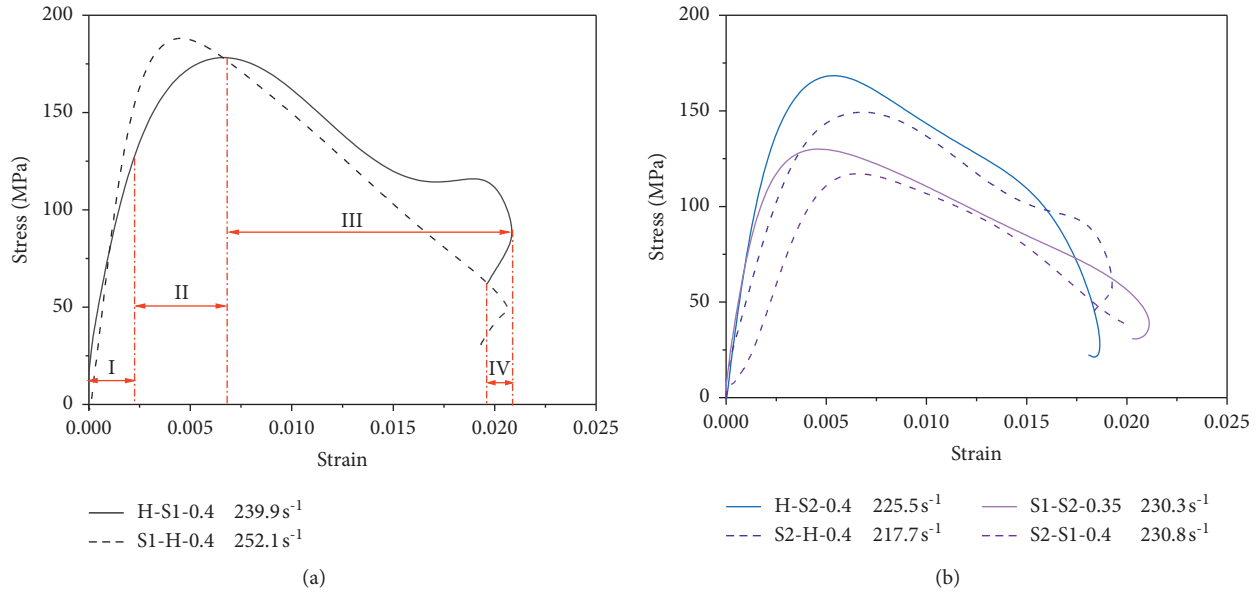

Figure 6: Typical dynamic stress-strain curves of composite specimens. (a) H-S1, (b) H-S2, and S1-S2 with similar strain rates.

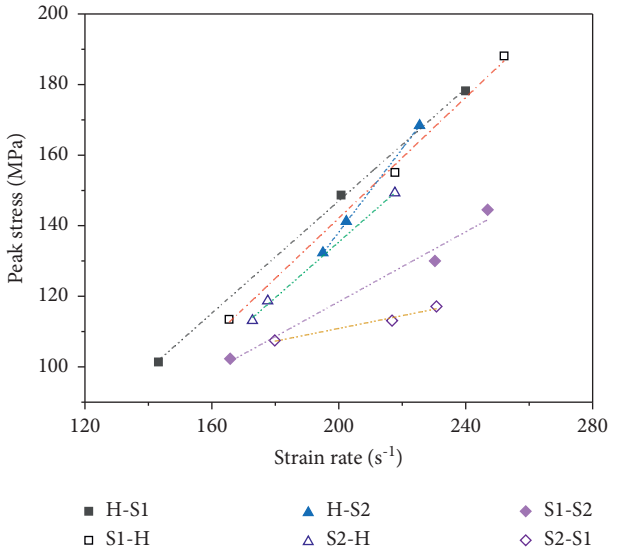

Figure 7: Relationship between peak stress and strain rate.

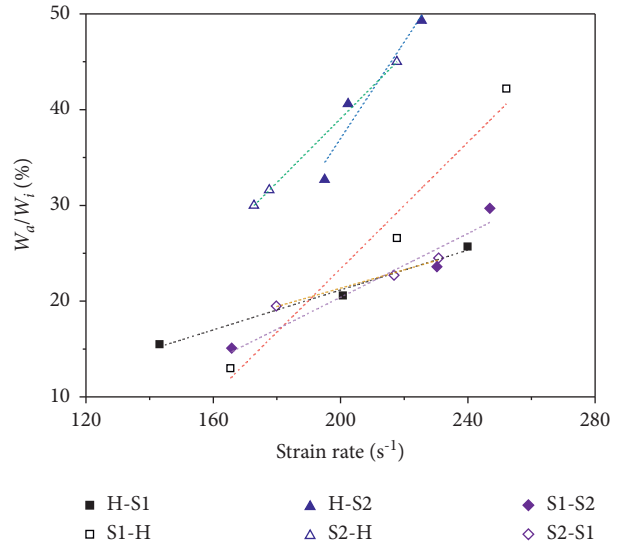

Figure 8: Variations of energy absorption rate versus strain rate.

stresses are listed in Table 2. The scatter of the data points in Figure 7 represents that the front and back of the composite sample are the rock with higher UCS. As shown in Figure 7, the peak stresses of all the composite samples are positively correlated with the strain rate, i.e., the greater the strain rate, the larger is the peak stress. On the whole, the dynamic strength of the composite with higher UCS rock in the front is higher, i.e., the composite is not easy to fail when the incident stress wave first passes through the relatively hard rock; on the contrary, it is easy to fail. For the composite samples H-S1 and S1-H, the sensitivity of the peak stress to the strain rate is the same, showing that the slope of the linear fitting line is the same. However, the strain rates corresponding to the composite samples S1-H are generally larger than that of H-S1. For the combination of H-S2 and S2-H, the strain rates of H-S2 are large, and the dynamic strength is more sensitive to the variation of strain rate, i.e., a small variation of strain rate can lead to a large change in strength. Finally, the variation of the peak stresses of S1-S2 and S2-S1 with strain rate is consistent with that of H-S2 and S2-H.

3.2. Energy Consumption. According to the energy calculation formula in Section 2.3.2, the W_i, W_t, W_r, and W_a of the composite specimen can be obtained. The specific values of the energy absorption rate (EUR, $\eta = W_a/W_i$) were also listed in Table 2, which can be used to analyze the energy dissipation characteristics of the composite specimen under dynamic loads. Figures 8 and 9 show the corresponding variation of the EUR for the composite sample with the strain rate and incident energy, respectively. As shown in

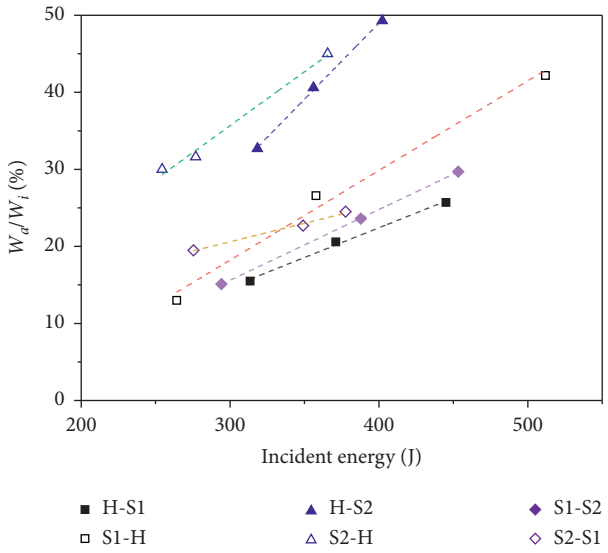

Figure 9: Variations of energy absorption rate versus incident energy.

Figure 8, for different combinations, the increase in strain rate enhances the EUR of the combination, and the increment of EUR is approximately linear with the strain rate. The values of EUR for different combinations (such as H-S1 and S1-H) are nonstationary, i.e., within a certain strain rate range (such as $160\,s^{-1}$–$200\,s^{-1}$), the EUR of a certain combination (such as S1-H) is large, and after exceeding the limit value of strain rate, the EUR of another combination (H-S1) is high. The other combinations (H-S2, S2-H, and S1-S2, S2-S1) also follow the same variation trend. As shown in Figure 9, the incident energy is also linear and positively correlated with the EUR of the combination. The variation trend of the EUR for the combination under different incident energy is stronger than that of strain rate. When the incident energy is the same, the EUR of the combination S1-H, S2-H, and S2-S1 is higher. The rock with low strength first contacts with the incident stress wave that enhances the EUR of the combination.

3.3. Failure Process and Displacement Field

3.3.1. Failure Process. Figure 10(a) shows the high-speed photographs of the failure process of H-S1 and S1-H under different gas pressures. As shown in Figure 10, there is a significant difference in the dynamic failure process of the combination form of front soft rear hard (FSRH) and front hard rear soft (FHRS). Also, the gas pressure greatly influences the failure mechanism. When the gas pressure is small, the failure of the combination H-S1-0.3 is overall more severe than that of S1-H-0.3. Furthermore, the cyan sandstone of H-S1-0.3 first generated many vertical cracks to divide the rock into blocks, and then, severe ejection occurred. However, granite was destroyed only under the secondary action of the incident bar after the failure of the cyan sandstone. On the other hand, although the strain rate of the combination S1-H-0.3 is large, granite and cyan sandstone only had a slight failure at the edge, and the bonding part of the two lithologies was separated. Furthermore, with the increase in the incident gas pressure, the granite also began to fail, such as the combination H-S1-0.35. Under the impact, the cyan sandstone first failed locally, and then, the vertical cracks were found in the middle of the combination sample. Finally, the cyan sandstone blocks were severely ejected, and the granite only produced fragments falling in the local area.

The failure of the composite S1-H-0.35 was similar to that of H-S1-0.35, while the failure of the cyan sandstone with low strength occurred first. The crack position on the granite surface corresponds to the crack of the cyan sandstone, forming a penetrating crack at a certain angle with the incident direction. When the gas pressure reached a large value, the granite started exhibiting severe ejection phenomena, such as the combination S1-H-0.4. However, it is still the first failure of the cyan sandstone. On the contrary, the combination H-S1-0.4 only increased the fragmentation of cyan sandstone, whereas the granite did not show obvious fragmentation characteristics, which was related to the low strain rate. Therefore, no matter for the combination of FSRH or FHRS, the rock with low strength failed first under impact loads, and whether the rock with high strength primarily fails depends on the incident energy. When the incident energy is large enough, more severe failure may occur.

Figure 10(b) shows the dynamic failure process of the combinations S1-S2 and S2-S1. In the combination of granite and cyan sandstone, the granite UCS is about 3.5 times that of cyan sandstone and that of cyan sandstone is about 1.5 times that of red sandstone. Therefore, the difference in the properties of the two rocks in the combination of S1-S2 is small, and the failure mechanism is quite different from that of the H-S combination. In particular, when the gas pressure is small, the red sandstone of the combination S1-S2-0.3 fails in local areas and produces transverse cracks near the bonding surface. However, the cyan sandstone and red sandstone of combination S2-S1-0.3 both failed, while the failure of the cyan sandstone was more intense. The red sandstone has only one vertical crack, which is simultaneously generated with the crack of the cyan sandstone, and the debonding phenomenon occurs. Additionally, for the combination S1-S2-0.35, due to the increase in the incident gas pressure, the ejection phenomenon of red sandstone is more intense, and the cyan sandstone only appears with surface cracks. When the gas pressure increases again, such as the combination S1-S2-0.4, the incident energy increases, and the failure of red sandstone is not sufficient to consume all the energy. The failure of cyan sandstone consumes the redundant energy, so the cyan sandstone has a relatively severe failure, and the surface crack propagation gradually develops into the ejection of the blocks. Also, for the combinations S2-S1-0.35 and S2-S1-0.4, the failure of red sandstone and cyan sandstone is relatively small. Only the transverse tensile cracks perpendicular to the incident direction are generated in red sandstone, primarily due to the propagation of the tensile stress wave generated by reflection in red sandstone.

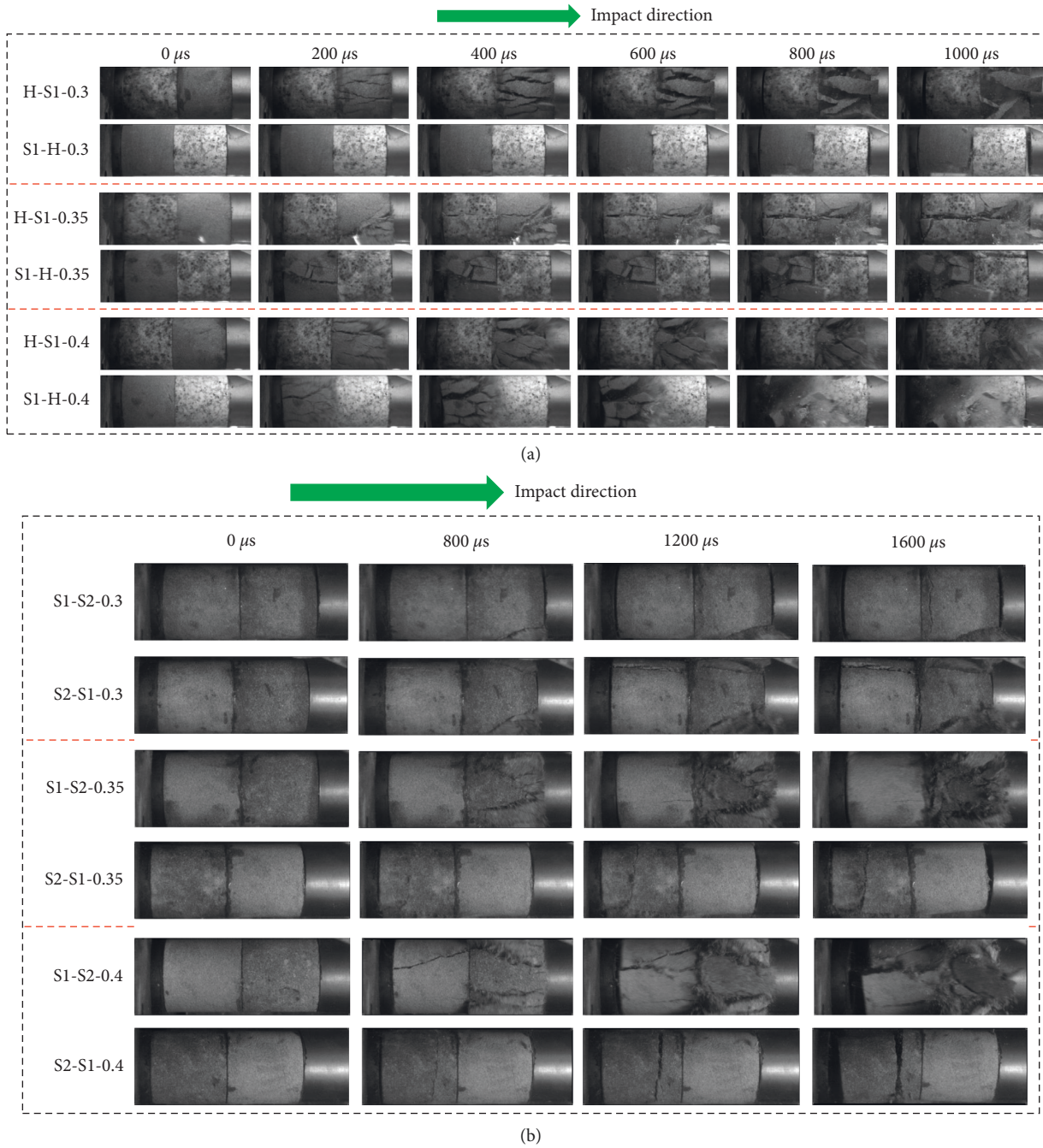

Figure 10: Failure processes of composite specimens under different strain rate loadings. (a) H-S1 and (b) S1-S2.

Therefore, on the whole, for different combinations, when the mechanical properties of the rocks constituting the combination are quite different, no matter which of the incident stress waves first contact with the relatively hard or the soft rock, the failure always occurs in the soft rock. When the energy carried by the dynamic load is large enough, the failure of the soft rock is not sufficient to consume all the energy, and the hard rock will consume the redundant energy. However, when the difference in rock strength of combination is small, the order of contact between incident stress wave and relatively hard or soft rock in the combination has a greater influence on the failure mode. When the combination is first contacted with soft rock, the overall failure of the combination is weaker, and the soft rock plays a critical role in absorbing energy and restricting the energy transfer. Therefore, it provides a reference for preventing and controlling dynamic disasters such as rock bursts in deep-buried hard rock tunnels.

3.3.2. Full-Displacement Fields. According to the principle of digital image correlation, the full-field displacement of the specimen before failure was obtained. As shown in Figures 11 and 12, the horizontal and vertical displacement fields on the surface of H-S1 and S1 -S2 specimens are,

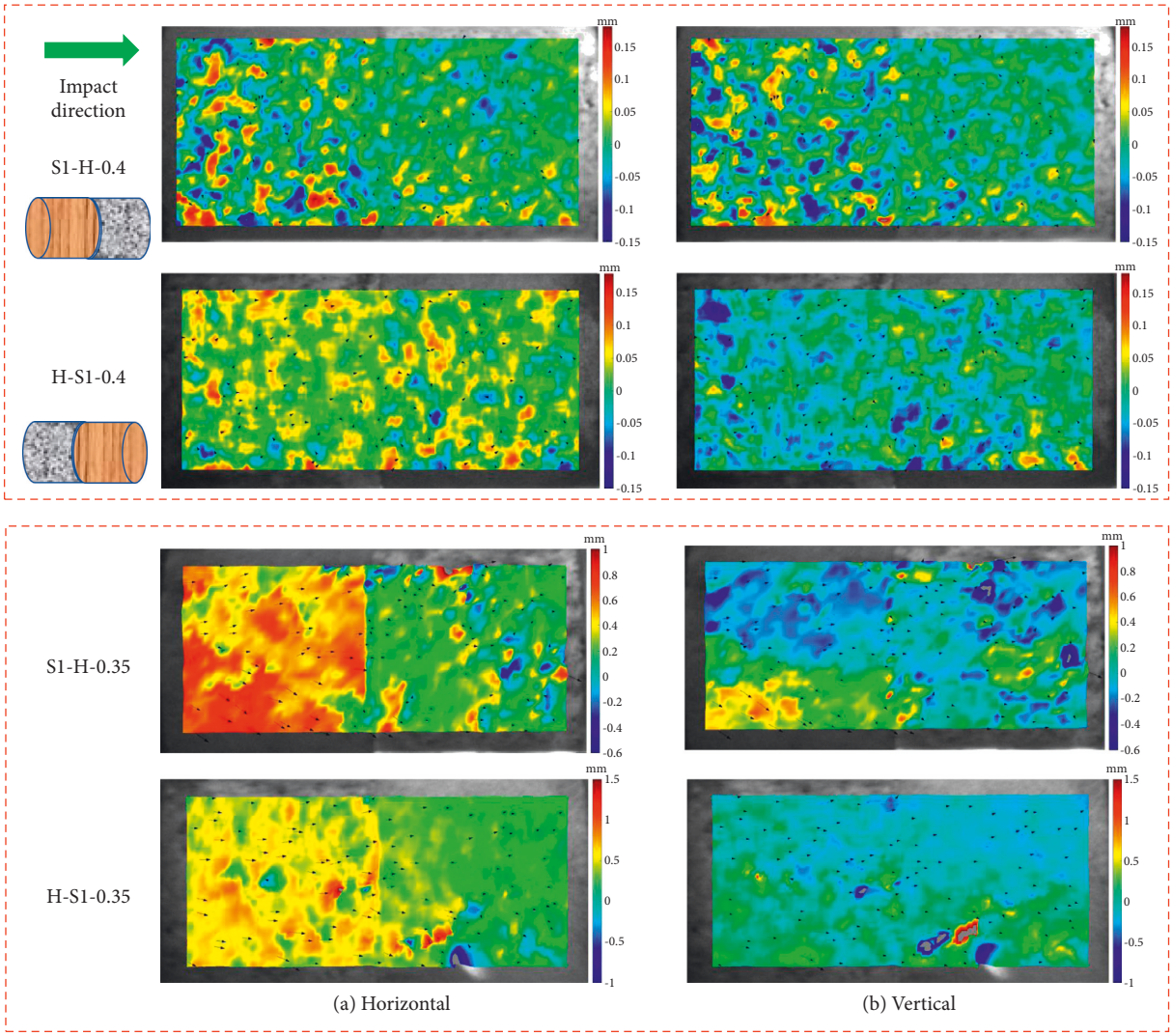

Figure 11: (a) Horizontal and (b) vertical displacement fields of composite samples H-S1.

respectively, shown, and the right and downward are positive directions, respectively, for horizontal and vertical. As shown in Figure 11, the horizontal and vertical displacement of cyan sandstone in the composite S1-H-0.4 is larger than that of granite, i.e., the cyan sandstone first produces large compression deformation under the action of the incident wave. The main deformation of the composite in the early stage is derived from cyan sandstone. Compared to S1-H-0.4, the horizontal and vertical displacement fields of H-S1-0.4 are evenly distributed in the two lithologies, and the displacement vector shows the same variation trend: the displacement of relatively soft rock is more concentrated. Furthermore, when the gas pressure is 0.35 MPa, the above characteristics of the displacement field are more noticeable. For example, the horizontal displacement field has an obvious boundary in the combination S1-H-0.35, which corresponds to the position of the bonding section of the combination. In general, the horizontal displacement of the whole cyan sandstone is to the right, while the horizontal displacement (less than that of the cyan sandstone) of the granite in a local area is to the left. In addition, an obvious crack propagation line can be seen in the vertical displacement field, and the vertical movements of the rock above and below the line are opposite.

As shown in Figure 12, for the composite rock with a small strength disparity, the rock contacted with the incident wave first generates large horizontal displacement under the impact load with different strain rates. The increase in gas pressure will increase the coverage area of a relatively large displacement zone but will not affect the horizontal displacement direction (right) of the composite sample. Additionally, when the impact gas pressure is equal, the horizontal displacement produced by the combination of FSRH is larger than that produced by the combination of FHRS. Compared with the horizontal displacement, the vertical displacement is smaller, and the displacement vector only has the vertical component in the local area. The boundary between the upward and downward movements

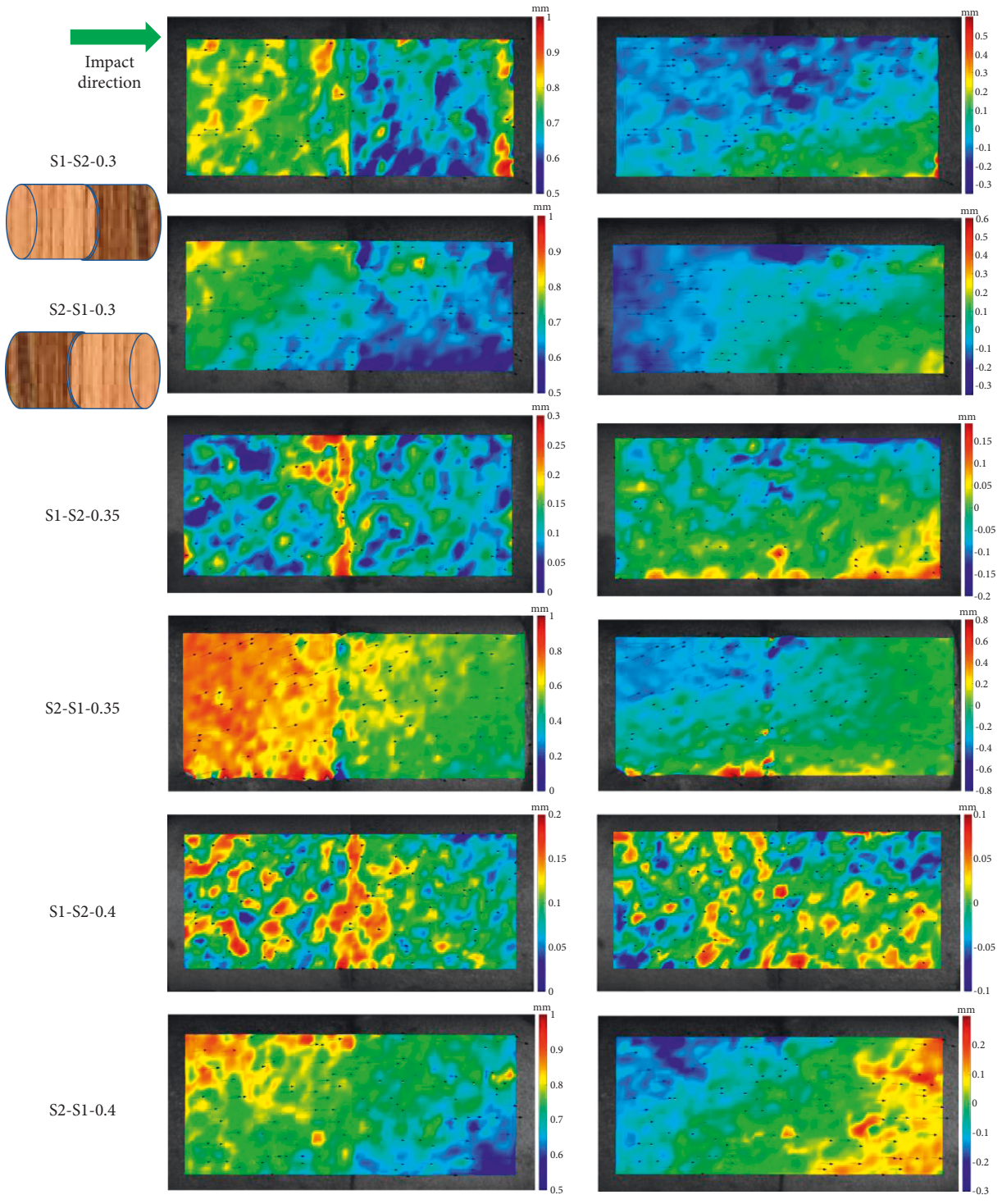

(a) Horizontal (a) Vertical

Figure 12: (a) Horizontal and (b) vertical displacement fields of composite samples S1-S2.

of the combination is irregular. Therefore, when the rock strength of the composite is highly different, the rock with lower strength is the main bearing carrier of the deformation under impact loads. However, when the difference between the two rocks of composite is small, the deformation is jointly borne by the two parts, though the deformation of the FSRH is larger.

3.4. Fragments Characteristics

3.4.1. Failure Features. Figure 13 shows the images of the fragments with particle size greater than 5 mm after impact. The increase in strain rate will aggravate the degree of fragmentation of the combination. When the strain rate is small, the residual parent body maintains a relatively

Figure 13: Failure photographs of composite samples after impact of dynamic loadings.

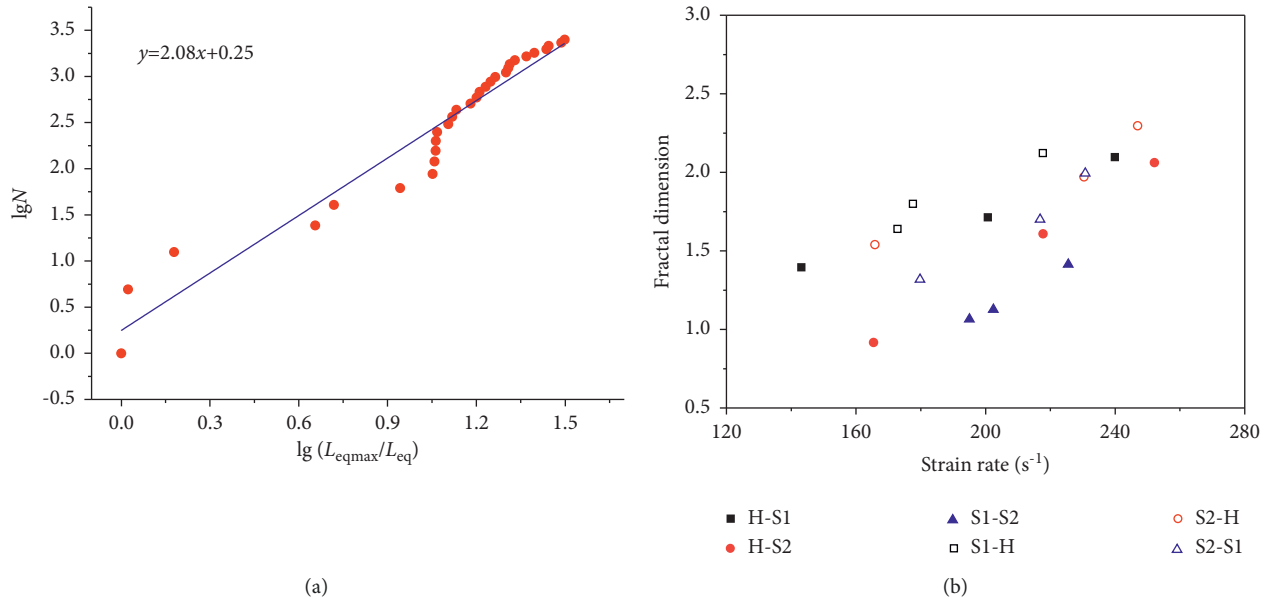

Figure 14: (a) Diagram of fractal dimension calculation, and (b) variations of fractal dimension of different composite samples with strain rate.

complete shape, and the soft rock in the combination appears in the bullet-head blocks (H-S1-0.3). With the increase in strain rate, the hard rock in the combination is also broken into large blocks, and the bonding interface of the two lithologic rocks in the combination is almost intact. Moreover, comparing the combinations H-S1 and H-S2, it can be seen that the greater the strength disparity between the two lithologic rocks in the combination, the more severe is the final fragmentation, i.e., the fragmentation of H-S2 is more severe than that of S2-H. In contrast, when the difference in rock properties in the combination is small, the fragmentation degree of the combination is more controlled by strain rate and has little relationship with the combination form.

3.4.2. Fractal Dimension. The fractal dimension (FD) of the fragments can reflect the fragmentation characteristics. In this study, the FD is determined using the particle size number calculation method. The fragments (greater than 5 mm) were equivalent to a cube. According to the measured length (l), width (w), and thickness (h) of the fragments (the above three values were the maximum values in three directions), the equivalent edge length L_{eq} of the cube was obtained, and the corresponding FD was calculated according to equation (6), reference [43].

$$N = N_0\left(\frac{L_{eq}}{L_{eq\,max}}\right)^{-D}, \tag{6}$$

where L_{eq} equals $(l \times w \times h)^{1/3}$; N is the number of fragments in the selected scale with L_{eq} less than L_{eq}; N_0 is the number of fragments corresponding to the L_{eqmax}; and D is the FD value. When the $\lg(L_{eqmax}/L_{eq})$ and $\lg N$ are the horizontal and vertical coordinates, respectively, the slope of the fitting straight line is the FD, as shown in Figure 14(a).

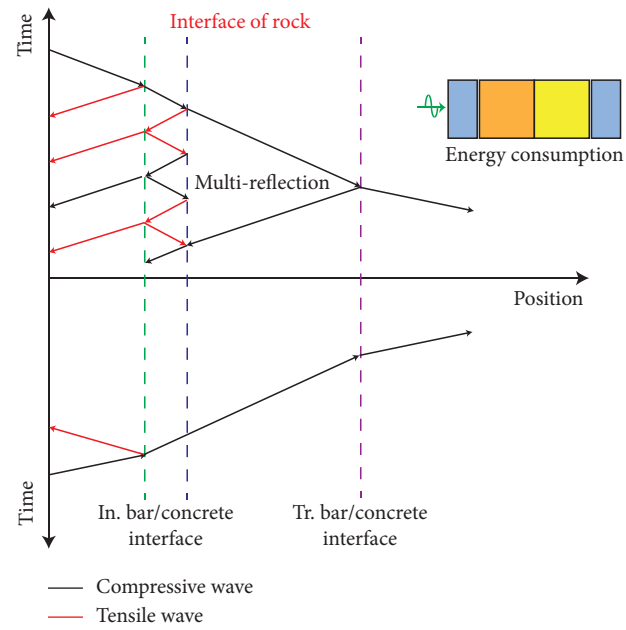

Figure 15: Diagram of stress wave propagation at the interface of composite (After Pothnis, 2018).

Figure 14(b) shows the variation of FD with strain rate for different combinations. As shown in Figure 14, the FD of all the composite samples is directly correlated with the strain rate, i.e., the larger the strain rate, the larger is the FD. Additionally, the larger the FD value, the smaller is the difference in the characteristic size of the fragment, i.e., the closer is the fragmentation scale of the fragment. Therefore, the shape of the fragment is closer to the combination with FSRH. The shape difference between the fragments is small, indicating that the propagation of stress waves in the specimen is more uniform, and the energy dissipation and absorption effect is better.

3.5. Failure Mechanism. According to the one-dimensional stress wave principle, as shown in Figure 15, reference [44], there is reflection and transmission of stress waves at the interface of the composite sample. The reflection wave is a tensile wave, and the incident wave and transmission wave are compression waves. The combination with FSRH rocks is more likely to cause new cracks under the action of multiple reflection tensile stress waves due to the lower tensile strength of the front rock, and then expands and penetrates to form macroscopic cracks, resulting in final failure. Hence, the front soft rock plays a vital role in blocking and attenuating the propagation of stress waves, and this phenomenon does not easily occur if the front rock is hard. In addition, the energy-blocking effect is obvious when the strength difference between the front and the rear rocks is large. If the tensile properties of the front and rear rock are not different, the integrity of the composite sample is better, and the probability of overall failure is large.

4. Conclusions

In order to investigate the dynamic mechanical behavior of deep-buried tunnel composite rock mass, the SHPB tests of three kinds of lithologies and six kinds of composite forms were carried out in this study. The influences of the combination form and strain rate on the stress-strain curve, peak stress, EUR, failure process, displacement field, and failure mode of the composite sample were analyzed. The main conclusions drawn from the results are as follows:

(1) The peak stress of all the combinations is linearly and positively correlated with the strain rate. When the strain rate is close, the peak stress and elastic modulus of the combination with FHRS rocks are larger. However, the sensitivity of different combinations to the strain rate is different.

(2) The EUR of different combinations is proportional to the incident energy, and the EUR of the FSRH combination is generally higher than that of the RHRS combination.

(3) Under the action of dynamic load, the rock with low strength always fails first in the composite. When the strength difference between the two rocks constituting the composite is small, the failure of the composite with FSRH is relatively small, and the main deformation before the failure occurs in the rock with low strength.

(4) The FD of the fragments after the impact of the FSRH combination is larger, and the lumpiness is closer, i.e., the failure is more uniform.

Data Availability

All data used during the study are available from the corresponding author by request.

Conflicts of Interest

The authors declare that they have no conflicts of interest.

Acknowledgments

Financial support received from the Education Department of Liaoning Province (grant no. 601009890-07) is gratefully acknowledged.

References

[1] W. Broere, "Urban underground space: s's cities," *Tunnelling and Underground Space Technology*, vol. 55, pp. 245–248, 2016.

[2] S. Q. Yang, M. Chen, H. W. Jing, K. F. Chen, and B. Meng, "A case study on large deformation failure mechanism of deep soft rock roadway in Xin'An coal mine, China," *Engineering Geology*, vol. 217, pp. 89–101, 2017.

[3] J. Wang, B. Yu, H. Kang et al., "Key technologies and equipment for a fully mechanized top-coal caving operation with a large mining height at ultra-thick coal seams," *International Journal of Coal Science & Technology*, vol. 2, no. 2, pp. 97–161, 2015.

[4] M. Gao, J. Xie, J. Guo, Y. Lu, Z. He, and C. Li, "Fractal evolution and connectivity characteristics of mining-induced crack networks in coal masses at different depths," *Geomechanics and Geophysics for Geo-Energy and Geo-Resources*, vol. 7, no. 1, p. 9, 2021.

[5] X. Zhang, J. Cheng, and C. Shi, "Damage assessment for underground brick seal under explosion impact load," *Arabian Journal of Geosciences*, vol. 14, no. 5, p. 391, 2021.

[6] Q. Wang, M. He, S. Li et al., "Comparative study of model tests on automatically formed roadway and gob-side entry driving in deep coal mines," *International Journal of Mining Science and Technology*, vol. 31, no. 4, pp. 591–601, 2021.

[7] G. Li, Y. Hu, S. m. Tian, and M. H.-l. weibin, "Analysis of deformation control mechanism of prestressed anchor on jointed soft rock in large cross-section tunnel," *Bulletin of Engineering Geology and the Environment*, vol. 80, no. 12, pp. 9089–9103, 2021.

[8] T. b. Zhao, W. y. Guo, Y. l. Tan, C. p. Lu, and C. w Wang, "Case histories of rock bursts under complicated geological conditions," *Bulletin of Engineering Geology and the Environment*, vol. 77, no. 4, pp. 1529–1545, 2018.

[9] X. Li, Q. Li, Y. Hu et al., "Study on three-dimensional dynamic stability of open-pit high slope under blasting vibration," *Lithosphere*, vol. 2021, no. 4, Article ID 6426550, 2022.

[10] C. Zhu, M. Karakus, M. He et al., "Volumetric deformation and damage evolution of Tibet interbedded skarn under multistage constant-amplitude-cyclic loading," *International Journal of Rock Mechanics and Mining Sciences*, vol. 152, Article ID 105066, 2022.

[11] Y. q. Su, F. q. Gong, S. Luo, and Z. x Liu, "Experimental study on energy storage and dissipation characteristics of granite under two-dimensional compression with constant confining pressure," *Journal of Central South University*, vol. 28, no. 3, pp. 848–865, 2021.

[12] Z. j. Wu, Z. y. Wang, L. f. Fan, L. Weng, and Q. s. Liu, "Micro-failure process and failure mechanism of brittle rock under uniaxial compression using continuous real-time wave velocity measurement," *Journal of Central South University*, vol. 28, no. 2, pp. 556–571, 2021.

[13] Z. Tao, Q. Geng, C. Zhu et al., "The mechanical mechanisms of large-scale toppling failure for counter-inclined rock slopes,"

Journal of Geophysics and Engineering, vol. 16, no. 3, pp. 541–558, 2019.

[14] M. Z. Gao, B. G. Yang, J. Xie et al., "The mechanism of microwave rock breaking and its potential application to rock-breaking technology in drilling," *Petroleum Science*, 2022.

[15] Z. Dou, S. Tang, X. Zhang et al., "Influence of shear displacement on fluid flow and solute transport in a 3D rough fracture," *Lithosphere*, vol. 2021, no. 4, Article ID 1569736, 2021.

[16] Z. Dou, Y. Liu, X. Zhang et al., "Influence of layer transition zone on rainfall-induced instability of Multilayered slope," *Lithosphere*, vol. 2021, no. 4, Article ID 2277284, 2021.

[17] D. Chen, H. Chen, W. Zhang, J. Lou, and B. Shan, "An analytical solution of equivalent elastic modulus considering confining stress and its variables sensitivity analysis for fractured rock masses," *Journal of Rock Mechanics and Geotechnical Engineering*, vol. 14, no. 3, pp. 825–836, 2021.

[18] J. Liu, E. Wang, D. Song, S. Wang, and Y. Niu, "Effect of rock strength on failure mode and mechanical behavior of composite samples," *Arabian Journal of Geosciences*, vol. 8, no. 7, pp. 4527–4539, 2015.

[19] Y. Wang, H. N. Yang, J. Q. Han, and C. Zhu, "Effect of rock bridge length on fracture and damage modelling in granite containing hole and fissures under cyclic uniaxial increasing-amplitude decreasing-frequency (CUIADF) loads," *International Journal of Fatigue*, vol. 158, Article ID 106741, 2022.

[20] B. Pan, W. Yu, and W. Shen, "Experimental study on energy evolution and failure characteristics of rock-coal-rock combination with different height ratios," *Geotechnical & Geological Engineering*, vol. 39, no. 1, pp. 425–435, 2021.

[21] T. Li, G. Chen, Y. Li, and Q. Li, "Study on progressive instability characteristics of coal-rock composite structure with the different height ratios," *Geotechnical & Geological Engineering*, vol. 40, no. 3, pp. 1135–1148, 2021.

[22] Y. Tao, L. Zhenhua, C. Zhiheng, Z. Quanle, C. Jialin, and H. Yanbo, "Deformation and failure characteristics of composite coal mass," *Environmental Earth Sciences*, vol. 80, no. 3, p. 114, 2021.

[23] Z. b. Cheng, L. H. Li, and Y. N. Zhang, "Laboratory investigation of the mechanical properties of coal-rock combined body," *Bulletin of Engineering Geology and the Environment*, vol. 79, no. 4, pp. 1947–1958, 2020.

[24] P. Zhang, D. Zhang, Y. Yang et al., "A case study on integrated modeling of spatial information of a complex geological body," *Lithosphere*, vol. 2022, no. Special 10, Article ID 2918401, 2022.

[25] X. S. Liu, Y. L. Tan, J. G. Ning, Y. W. Lu, and Q. H. Gu, "Mechanical properties and damage constitutive model of coal in coal-rock combined body," *International Journal of Rock Mechanics and Mining Sciences*, vol. 110, pp. 140–150, 2018.

[26] J. Zuo, H. Xie, and A. Wu, "Investigation on failure mechanisms and mechanical behaviors of deep coal-rock single body and combined body," *J Rock Mech Geotech*, vol. 30, pp. 84–92, 2011.

[27] W. Shen, W. Yu, B. Pan, and K. Li, "Rock mechanical failure characteristics and energy evolution analysis of coal-rock combination with different dip angles," *Arabian Journal of Geosciences*, vol. 15, no. 1, p. 93, 2022.

[28] Z.-G. Xia, S. Liu, Z. Bian, J. Song, F. Feng, and N. Jiang, "Mechanical properties and damage characteristics of coal-rock combination with different dip angles," *KSCE Journal of Civil Engineering*, vol. 25, no. 5, pp. 1687–1699, 2021.

[29] X. Tang, Q. Zhang, Y. Zhou, and D. Ma, "Damage and acoustic emission characteristics of combined rock mass with anchor under different inclination angles and combination modes," *Geotechnical & Geological Engineering*, vol. 39, no. 8, pp. 5895–5906, 2021.

[30] J. Lu, G. Huang, H. Gao, X. Li, D. Zhang, and G. Yin, "Mechanical properties of layered composite coal-rock subjected to true triaxial stress," *Rock Mechanics and Rock Engineering*, vol. 53, no. 9, pp. 4117–4138, 2020.

[31] W. Liu, W. Yuan, Y. Yan, and X. Wang, "Analysis of acoustic emission characteristics and damage constitutive model of coal-rock combined body based on particle flow code," *Symmetry*, vol. 11, no. 8, p. 1040, 2019.

[32] K. Ma and G. Liu, "Three-dimensional discontinuous deformation analysis of failure mechanisms and movement characteristics of slope rockfalls," *Rock Mechanics and Rock Engineering*, vol. 55, no. 1, pp. 275–296, 2022.

[33] Q. Zhang, X. Tang, Y. Zhou, and D. Ma, "Failure and acoustic emission characteristics of jointed rock masses with different joint inclination angles and combination mode," *Geotechnical & Geological Engineering*, vol. 39, no. 8, pp. 5971–5981, 2021.

[34] C. Li, Y. Xu, P. Chen, H. Li, and P. Lou, "Dynamic mechanical properties and fragment fractal characteristics of fractured coal-rock-like combined bodies in split Hopkinson pressure bar tests," *Natural Resources Research*, vol. 29, no. 5, pp. 3179–3195, 2020.

[35] L. Miao, Y. Niu, and B. Shi, "Impact dynamic tests for rock–coal–rock combination under different strain rates," *Journal of Vibration and Shock*, vol. 38, pp. 137–143, 2019.

[36] Y. Pan, Z. Li, and M. Zhang, "Distribution, type, mechanism and prevention of rockburst in China," *Chinese Journal of Rock Mechanics and Engineering*, vol. 22, pp. 1844–1851, 2003.

[37] J. Zuo, H. Xie, A. Wu, and J. Liu, "Investigation on failure characteristics and mechanical behavior of deep coal-rock single body and combined body under different confining pressures," *Chinese Journal of Rock Mechanics and Engineering*, vol. 30, pp. 84–92, 2011.

[38] S. n. Dong, A. Li, Y. d. Ji, Y. x. Yang, and Q. Mu, "Mechanical and failure characteristics of rock-coal-rock combined body under different strain rates: a numerical study from micro perspective," *Geotechnical & Geological Engineering*, vol. 39, no. 1, pp. 185–191, 2021.

[39] Z. Lu, W. Ju, F. Gao, and K. Yi, "Influence of loading rate on the failure characteristics of composite coal-rock specimens under quasi-static loading conditions," *Rock Mechanics and Rock Engineering*, vol. 55, no. 2, pp. 909–921, 2022.

[40] S. Xie, M. Huang, J. Lu, W. Xi, and Z. Xu, "Experimental investigation on the energy consumption difference between the dynamic impact and the drilling tests of rocks," *Shock and Vibration*, vol. 2022, pp. 1–15, Article ID 3729822, 2022.

[41] Z. Zhou, X. Cai, X. Li, W. Cao, and X. Du, "Dynamic response and energy evolution of sandstone under coupled static-dynamic compression: insights from experimental study into deep rock engineering applications," *Rock Mechanics and Rock Engineering*, vol. 53, no. 3, pp. 1305–1331, 2020.

[42] Z. Yan, F. Dai, Y. Liu, and H. Du, "Experimental investigations of the dynamic mechanical properties and fracturing behavior of cracked rocks under dynamic loading," *Bulletin of*

Engineering Geology and the Environment, vol. 79, no. 10, pp. 5535–5552, 2020.

[43] Y. Wang, Z. Chun, M. He, D. Liu, and Y. S. Lin, "Fragmentation characteristics analysis of sandstone fragments for impact rockburst under different dynamic loading frequency," *Geotechnical & Geological Engineering*, vol. 37, no. 4, pp. 2715–2727, 2019.

[44] J. R. Pothnis, G. Ravikumar, H. Arya, C. S. Yerramalli, and N. K. Naik, "Stress wave attenuation in aluminum alloy and mild steel specimens under SHPB tensile testing," *Journal of Materials Engineering and Performance*, vol. 27, no. 2, pp. 677–686, 2018.